IET Electric Power Applications

Research Article

IET Journals
The Institution of Engineering and Technology

Rotor magnet demagnetisation diagnosis in asymmetrical six-phase surface-mounted AC PMSM drives

ISSN 1751-8660
Received on 1st March 2019
Revised 9th July 2019
Accepted on 7th October 2019
E-First on 17th July 2020
doi: 10.1049/iet-epa.2019.0222
www.ietdl.org

Yasser Gritli[1,2] ✉, Michele Mengoni[1], Gabriele Rizzoli[1], Claudio Rossi[1], Angelo Tani[1], Domenico Casadei[1]

[1]DEI – Department of Electrical, Electronic and Information Engineering 'Guglielmo Marconi', University of Bologna, Bologna 40126, Italy
[2]Department of Electrical Engineering, LARA-ENIT (LR-11-ES18), National Engineering School of Tunis University of Tunis El Manar, Tunis, Belvedere 1002, Tunisia
✉ *E-mail: yasser.gritli@unibo.it*

Abstract: Multiphase permanent-magnet synchronous machines (PMSMs) are receiving more and more interest in safety-critical modern industries owing to their higher reliability when compared with conventional three-phase PMSMs. Rotor magnets are critical components, which, in case of fault, directly affect the performance of the PMSMs. Thus, monitoring the rotor magnets status is essential to ensure both high level of efficiency and service continuity. The present study focuses on the investigation of a new approach for the detection of rotor magnet demagnetisation in a vector-controlled asymmetrical six-phase surface-mounted AC PMSM. The main contribution of the proposed technique is the assessment of a rotor demagnetisation fault index derived from the fifth and seventh harmonics of the stator voltage space vector evaluated in the α_5–β_5-plane, and already available in the control system platform. The performance of the proposed approach is evaluated using finite element analysis and numerical simulations, both validated by experimental tests.

1 Introduction

Multiphase permanent-magnets synchronous machines (PMSMs) have gained an impressive interest during the last decade as a potential alternative to their three-phase PM machine counterparts, for safety-critical variable-speed drive applications as well as high-power energy conversion systems [1]. The main motivation of this interest is to combine the merit of high-torque/power switch rating of the PM machines [2], with additional degrees of freedom, which are increasing with the number of phases, leading to a significant increase of efficiency and fault tolerability of the machine [3–5]. These advantages are of paramount importance for modern wind energy conversion systems [6], aerospace, or 'more electric aircraft' concept [7], where high-reliability standards are required.

Although the advantages of multiphase AC PMSMs in terms of stator fault tolerance as they can operate even with one or more faulty phases, they remain potentially predisposed to rotor magnets demagnetisation (RMsD), similarly to three-phase PM machines.

Demagnetisation phenomenon is a combination of mechanical, electrical, and mainly thermal stresses [8]. RMsD is a reversible phenomenon, which can evolve progressively either under overload operating conditions or under fault conditions becoming completely irreversible [8, 9].

Magnetic properties of all the permanent materials change with temperature. In materials such as neodymium, iron, and boron and samarium–cobalt, remanence as well as coercivity decrease with increasing temperature.

Besides this, the variation in armature resistance of the motor due to the temperature increase has a temporary impact on the torque capabilities of the PM motor. As the temperature decreases, intrinsic coercivity and residual flux density will return to the initial values, leading to a normal reversible demagnetisation phenomenon. However, once the working temperature of the rotor magnets exceeds a certain level, related to their intrinsic properties, the magnet is weakened permanently, and the initial flux density level cannot be reached anymore even if the temperature is decreased. More specifically, the no-load back-electromotive force (EMF) of the motor will be reduced, and the required current for rated operating conditions will increase, leading to a further temperature rise and then to an irreversible RMsD. Thus, monitoring the rotor magnets status is essential to prevent irreversible RMsD and permanent performance reduction of PMSMs.

Being three-phase machines considered the workhorse in a wide range of industrial applications for a long time, a large variety of effective RMsD diagnosis techniques devoted to three-phase PMSMs have been developed [10–21]. On the basis of low-cost Hall effect sensors, a non-invasive technique for estimating the rotor PM temperature without a priori motor parameter information is presented in [12]. In [13], a pulsating high-frequency current injection method is developed.

A practical thermal model-based technique is presented in [14], where a simplified thermal lumped element network model, using only two time constants, is presented for estimating the temperatures of PMs and stator windings. Differential inductance pattern due to the variation of magnetic saturation is used in [15] for detecting RMsD.

Mechanical signal-based techniques using spectral torque analysis [16, 17], vibration signature analysis [18], or direct measurements of shaft trajectory performed using a non-contact self-mixing interferometric sensor [19] have shown significant performance for detecting RMsD. However, incurred cost and/or the invasive installation required for measurements are limits to the applicability of these techniques. To cope with these issues, different electrical signal-based approaches have been investigated, namely stator currents signature analysis [16], zero-sequence voltage component [20], or back EMF [21] have been developed for extracting effective RMsD fault signatures.

Causes of RMsD are not limited to overload operating conditions, but can be potentially produced by stator windings or inverter faults, even in case of multiphase PM machines well known as highly reliable against stator faults. Several scenarios of stator fault as shorting or opening of one or more of stator phase windings can lead to drastic propagation of the demagnetising effect. Thus, for preventing serious RMsD, the number of developed stator fault detection and tolerance techniques for multiphase AC PM machines based on multiple three-phase windings sets makes sense [1, 4, 5, 22].

Although the important advances in diagnosis and fault-tolerance techniques of stator anomalies dedicated to multiphase PM machines, RMsD has not received up to now the attention that deserves. To the best of authors' knowledge, and the available

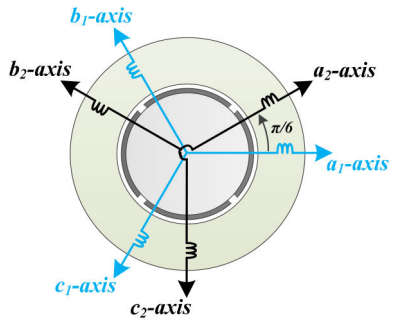

Fig. 1 *Six-phase surface-mounted AC PMSM with a spatial shifting of π/6 between the two sets of three-phase windings and separate neutral points*

literature, a relatively few papers have investigated possible RMsD fault index devoted to multiphase PMSMs. The EMF space-vector behaviour has been proposed for continuous online monitoring of RMsD in five-phase AC PMSG drives in [23, 24]. More specifically, RMsD can be identified by analysing the voltage references generated by multi-reference frame current regulators, which are used to implement a field-oriented control (FOC) scheme. On the basis of the RMsD detection process, a robust FOC scheme was developed showing undisturbed system under faulty conditions. Assessment of current and voltage signature analyses for the diagnosis of RMsD in five-phase AC PMSG drive has been established in [25].

Among different topologies, multiphase AC PM machines based on multiple three-phase winding sets are becoming more and more popular, since the modularity of the structure and the reliability of the associated standard three-phase inverters are assumed a mature technology.

Specifically, asymmetric six-phase AC PM motors are of interest because a dual three-phase winding, having a spatial shift of $\pi/6$ and common or separate neutral point, could be housed in the stator of the same three-phase PM machine [6, 26]. Recently, RMsD fault signature based on back-EMF analysis has been experimentally validated for asymmetric six-phase AC PM motors [27, 28].

In this paper, the specific demagnetisation of the trailing edges of all the rotor magnets is analysed. This phenomenon can take place in case of overcurrent, when the common FOC technique is adopted. The air-gap distribution of the stator MMF is maintained maximum along the quadrature axis, and under these conditions, half of each magnet can be over reverse magnetised, leading to demagnetisation of the trailing edge. The proposed RMsD detection technique is based on the analysis of the stator voltage space-vector harmonic references in the accessible α_5–β_5-plane. The presented results can be considered as a continuity of the investigations presented in [27], and then in [28], by an experimental implementation and validation of the proposed RMsD diagnosis process.

This paper is organised as follows. Section 2 reviews the modelling of the considered asymmetrical six-phase surface-mounted PMSM in terms of multiple space-vector representation (MSVR). This section is accompanied by two appendices providing a recall of the MSVR concept, and mathematical machine details. In Section 3, a motor signal-based detection technique is tested through finite element analysis (FEA) and experimentally validated thereby. Results corresponding to the proposed control signal-based approach for RMsD detection, which is first verified by numerical simulations then experimentally confirmed, are reported in Section 4. A description of the adopted control scheme and its experimental implementation are included in this section as well. In Section 5, a new fault index for RMsD quantification is presented and evaluated employing different fault levels.

2 MSVR-based modelling for six-phase surface-mounted PMSM

MSVR is an effective approach to simplify multiphase systems modelling with a well-designed and effective vectorial approach for real-time analysis of multiphase machines and drives. The MSVR principle allows modelling asymmetric six-phase AC surface-mounted PMSMs, by means of vectors in three α–β planes, where the direct and inverse linear transformations are recalled in Appendix 1 of Section 8.1. The considered machine is a six-phase surface-mounted PMSM, constituted by two sets of three-phase windings shifted by 30° (i.e. asymmetrical six-phase winding arrangement), as illustrated in Fig. 1. The starting point of the synthesised model is the evaluation of the total magnetic field in the air gap, due to stator currents and rotor magnets, in the stator reference frame, as detailed in Appendix 2 of Section 8.2.

The voltage equations, written in terms of MSVR, assume the following form:

$$\bar{v}_{S1} = R_S \bar{i}_{S1} + \frac{d\bar{\varphi}_{S1}}{dt} \tag{1}$$

$$\bar{v}_{S3} = R_S \bar{i}_{S3} + \frac{d\bar{\varphi}_{S3}}{dt} \tag{2}$$

$$\bar{v}_{S5} = R_S \bar{i}_{S5} + \frac{d\bar{\varphi}_{S5}}{dt} \tag{3}$$

where R_S is the stator phase winding resistance, $\bar{v}_{S1}$, $\bar{v}_{S3}$, and $\bar{v}_{S5}$ are the stator voltage space vectors and $\bar{i}_{S1}$, $\bar{i}_{S3}$, and $\bar{i}_{S5}$ are the stator current space vectors. In Appendix 2 of Section 8.2, it is shown how the linkage flux space vectors $\bar{\varphi}_{S1}$, $\bar{\varphi}_{S3}$, and $\bar{\varphi}_{S5}$ are evaluated, leading to the following expressions:

$$\bar{\varphi}_{S1} = L_{S1}\,\bar{i}_{S1} + \bar{\phi}_{m1}\,e^{j\theta} + \bar{\phi}_{m11}\,e^{-j\,11\theta} \tag{4}$$

$$\bar{\varphi}_{S3} = L_{S3}\,\bar{i}_{S3} + \bar{\phi}_{m3}\,e^{j\,3\theta} + \bar{\phi}_{m9}\,e^{-j\,9\theta} \tag{5}$$

$$\bar{\varphi}_{S5} = L_{S5}\,\bar{i}_{S5} + \bar{\phi}_{m5}\,e^{j\,5\theta} + \bar{\phi}_{m7}\,e^{-j\,7\theta} \tag{6}$$

Substituting (4)–(6) in (1)–(3), respectively, leads to the following voltage equations expressed in the stator reference frame as:

$$\bar{v}_{S1} = R_S \bar{i}_{S1} + L_{S1}\frac{d\bar{i}_{S1}}{dt} + j\,\omega\,\bar{\varphi}_{m1}\,e^{j\theta} - j\,11\,\omega\,\bar{\varphi}_{m11}\,e^{-j\,11\theta} \tag{7}$$

$$\bar{v}_{S3} = R_S \bar{i}_{S3} + L_{S3}\frac{d\bar{i}_{S3}}{dt} + j\,3\,\omega\,\bar{\varphi}_{m3}\,e^{j\,3\theta} - j\,9\,\omega\,\bar{\varphi}_{m9}\,e^{-j\,9\theta} \tag{8}$$

$$\bar{v}_{S5} = R_S \bar{i}_{S5} + L_{S5}\frac{d\bar{i}_{S5}}{dt} + j\,5\,\omega\,\bar{\varphi}_{m5}\,e^{j\,5\theta} - j\,7\,\omega\,\bar{\varphi}_{m7}\,e^{-j\,7\theta} \tag{9}$$

where $\omega = d\theta/dt$.

On the basis of the above voltage (7)–(9), the back EMFs can be expressed by (10)–(12), where the harmonic content in the α_1–β_1, α_3–β_3, and α_5–β_5 planes, respectively, are evidenced

$$\bar{e}_{S1} = j\,\omega\,\bar{\varphi}_{m1}\,e^{j\theta} - j\,11\,\omega\,\bar{\varphi}_{m11}\,e^{-j\,11\theta} \tag{10}$$

$$\bar{e}_{S3} = j\,3\,\omega\,\bar{\varphi}_{m3}\,e^{j\,3\theta} - j\,9\,\omega\,\bar{\varphi}_{m9}\,e^{-j\,9\theta} \tag{11}$$

$$\bar{e}_{S5} = j\,5\,\omega\,\bar{\varphi}_{m5}\,e^{j\,5\theta} - j\,7\,\omega\,\bar{\varphi}_{m7}\,e^{-j\,7\theta} \tag{12}$$

where θ is the rotor position in electrical radians.

Using a power balance, and based on the previous equations, the electromagnetic torque can be formulated by

$$\begin{aligned} T_{em} = {} & 3\,P\left[\bar{i}_{S1}\cdot j\,\bar{\varphi}_{m1}\,e^{j\theta}\right] + 9\,P\left[\bar{i}_{S3}\cdot j\,\bar{\varphi}_{m3}\,e^{j\,3\theta}\right] \\ & + 15\,P\left[\bar{i}_{S5}\cdot j\,\bar{\varphi}_{m5}\,e^{j\,5\theta}\right] + 21\,P\left[\bar{i}^{*}_{S5}\cdot j\,\bar{\varphi}^{*}_{m7}\,e^{j\,7\theta}\right] \\ & + 27\,P\left[\bar{i}^{*}_{S3}\cdot j\,\bar{\varphi}^{*}_{m9}\,e^{j\,9\theta}\right] + 33\,P\left[\bar{i}^{*}_{S1}\cdot j\,\bar{\varphi}^{*}_{m11}\,e^{j\,11\theta}\right] \end{aligned} \tag{13}$$

Note that, six contributions can be recognised. Two of them are related to the current space vector $\bar{i}_{S1}$, and two to the current space

Table 1 Six-phase surface-mounted AC PMSM parameters

Parameter	Value	Units
phase resistance	0.36	Ω
pole number	4	—
synchronous inductance space 1	7.2	mH
synchronous inductance space 5	0.74	mH
stator inner radius	150	mm
stator outer radius	240	mm
slot number	48	—
stator winding pitch	165°	el. deg
magnet pole arc	151°	el. deg
magnet radial thickness	5	mm

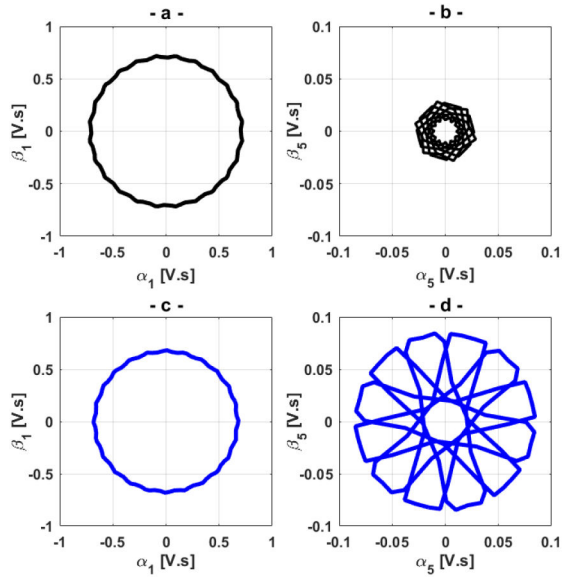

Fig. 2 *FEA results: loci of the back-EMF space vectors, in the α_1–β_1 and α_5–β_5 planes for six-phase PMSM prototypes*
(a), (b) Healthy, ***(c), (d)*** Under an RMsD of 10°

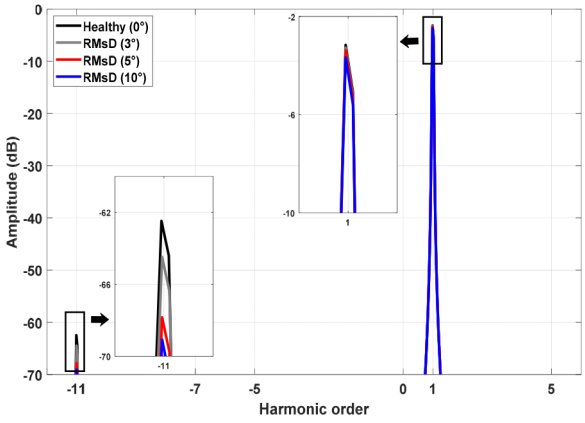

Fig. 3 *FEA results: harmonic spectra of the back-EMF space vectors in the α_1–β_1-plane, (black) healthy motor, (grey) 3° of RMsD, (red) 5° of RMsD, and (blue) 10° of RMsD*

vector $\bar{i}_{S5}$. Considering the machine design with separate neutral points, the remaining two contributions related to the current space vector $\bar{i}_{S3}$ are equal to zero.

The fourth and sixth contributions of (13) can lead to undesired torque pulsations. To obtain a smooth torque waveform, it is possible to set $\bar{i}_{S5}$ to zero, together with a proper machine design ensuring a negligible value of the phasor $\bar{\varphi}_{m11}$.

Finally, as the neutral points are isolated and thus the current space vector in the α_3–β_3-plane will be zero, the reported results in the following sections will be restricted to the analysis of the space vectors in the α_1–β_1 and α_5–β_5 planes.

3 Validation of motor signal-based detection technique of RMsD

In this section, the proposed RMsD fault signature is derived from back-EMF space vectors spectra. The performance of the proposed RMsD fault detection strategy has been preliminarily examined by two-dimensional FEA, and then experimentally confirmed.

3.1 FEA results

In this section, the simulation of a six-phase surface-mounted PMSM was carried out by FEA. The model of the machine under healthy and different RMsD cases was developed using finite element method and implemented in the FEMM© 4.2 software with dedicated LUA scripts.

A double-layer short pitch stator winding, shorted by one slot for compensating the 11th harmonic, is chosen. To minimise the cogging torque, and to reduce the contribution of the fifth and seventh harmonics in the EMFs under healthy conditions, a magnet pole arc of 151° was adopted. The main parameters of the considered healthy six-phase PMSM are listed in Table 1. Initially, the simulations have been conducted in no-load conditions at the rated speed, first with healthy magnets, then with rotor magnets having a reduced pole arc of 10° to emulate a demagnetisation on the trailing edges. Considering a FOC strategy, the stator MMF is maximum along the quadrature axis, and half of each magnet is reverse magnetised, leading to the so-called uniform demagnetisation phenomenon.

The obtained linkage fluxes under healthy and faulty conditions, computed in the FEMM environment, were imported thereby in MATLAB environment for space-vector elaboration in the α–β-plane, and spectral treatments. For the sake of fault sensitivity against the speed operating conditions, the EMFs have been normalised by the mechanical speed (rad/s). The loci references under healthy conditions, of the back-EMF space vectors in the α_1–β_1 and α_5–β_5 planes, are presented in Figs. 2*a* and *b*, respectively. The corresponding loci under an RMsD of 10° are reported in Figs. 2*c* and *d*. Comparing the results from healthy to the faulty case, the effect of the 10° of RMsD is evidenced in the α_5–β_5-plane, leading to a recognition pattern of the investigated fault.

Analysis of the back-EMF space vector in the α_5–β_5-plane provides direct information on the presence of RMsD, while the identification of spectral components, representative of RMsD in six-phase PMSMs, is an open problem. In this context, the spectral content of the back-EMF space vectors in the α_1–β_1 and α_5–β_5 planes have been investigated under 3°, 5°, and 10° of RMsD.

Fig. 3 shows the spectra of the back-EMF space vector, in the α_1–β_1-plane, for the healthy motor, and under different degrees of RMsD (3°, 5°, and 10°, respectively). It is clearly shown that the spectra are almost the same, under healthy and RMsD conditions, with a clear dominance of the fundamental, which confirm the circular behaviour of the loci reported in Figs. 2*a* and *c*, corresponding to the healthy case and for 10° of RMsD, respectively. Fig. 4 shows the spectra of the back-EMF space vector, in the α_5–β_5-plane, for the healthy case, and under the different degrees of RMsD. The amplitude variation of the inverse seventh harmonic, from healthy (black line) to a 10° of RMsD (blue line), can be evidenced. A much more relevant amplitude variation of the fifth harmonic is clearly evidenced from healthy to faulty (10° of RMsD) condition, leading to a potential fault component for RMsD detection. The above-discussed variations, of the inverse seventh and fifth harmonics from healthy to a 10° of RMsD, justify the loci behaviour evolution from Figs. 2*b*–*d*. Finally, considering the different increasing levels of RMsD, the fifth harmonic component has shown significant amplitude increments, respectively, leading to a sensitive index for RMsD.

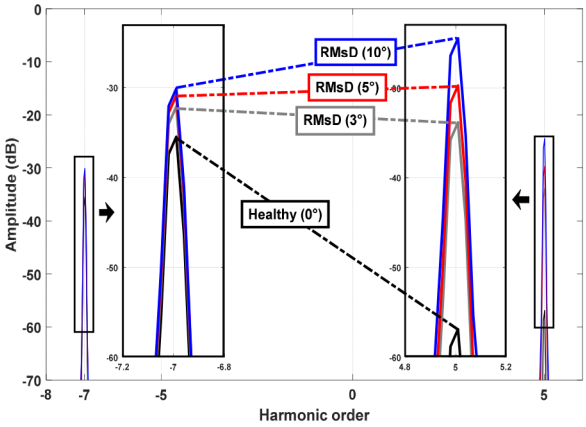

Fig. 4 *FEA results: harmonic spectra of the back-EMF space vectors in the α_5–β_5, (black) healthy motor, (grey) 3° of RMsD, (red) 5° of RMsD, and (blue) 10° of RMsD*

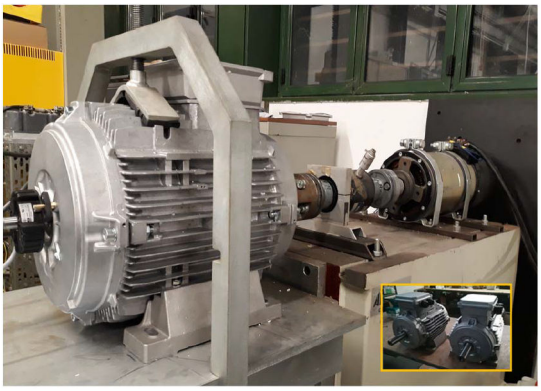

Fig. 5 *Laboratory test setup*

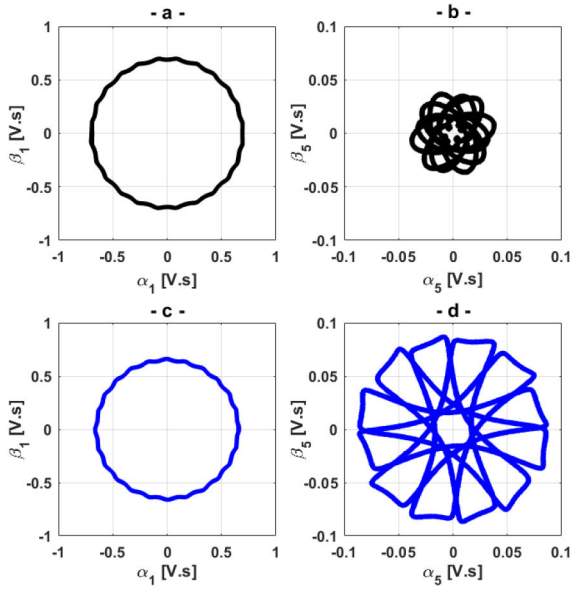

Fig. 6 *Experimental results: loci of the back-EMF space vectors, in the α_1–β_1 and α_5–β_5 planes for six-phase PMSM prototypes*

(a), (b) Healthy, ***(c), (d)*** Under an RMD of 10°

3.2 Experimental results

In this section, the proposed RMsD fault signature, derived from back-EMF space vectors, is experimentally tested in laboratory on two six-phase, surface-mounted, PMSM prototypes built for experiments (Fig. 5), where the main parameters of the healthy PMSM are listed in Table 1. For tests under faulty conditions, the second prototype has the same parameters as the healthy one (Table 1), but with a uniform RMsD of 10°.

The first series of tests have been performed in no-load conditions. The machine was driven by a 9 kW DC motor, fed by a commercial speed-controlled DC–DC drive that acts as a prime mover. For accurate spectral analysis, a high sampling rate (50 kHz) has been adopted for data acquisition. The back EMFs have been normalised with the mechanical speed (rad/s).

For space vectors elaboration in the α–β-plane (Fig. 6), and for spectral analysis (Figs. 7 and 8), all data has been imported in the MATLAB environment.

For reference tests, the healthy six-phase AC PMSM was run at rated speed (1000 rpm). The loci of the back-EMF space vectors evaluated in the α_1–β_1 and α_5–β_5 planes are reported in Figs. 6*a* and *b*, respectively. The corresponding spectra are reported in Figs. 7*a* and 8*a*, respectively. The circular behaviour of the back-EMF locus in the α_1–β_1-plane is justified by the relevance of the fundamental component evidenced in the spectrum of Fig. 7*a*, whereas the contribution of the fifth and inverse seventh harmonics observed in healthy conditions (Fig. 8*a*) justifies the behaviour of the locus in the α_5–β_5-plane corresponding to the healthy case.

Under the same no-load operating conditions, the second six-phase PMSM with a 10° of RMsD was run at the same constant speed. The resulting loci and spectra are reported in Figs. 6*c, d*, 7*b*, and 8*b*.

The loci of the back EMF in the α_1–β_1-plane, from healthy (Fig. 6*a*) to faulty conditions (Fig. 6*c*), show a quasi-similar circular behaviour with slightly reduced radius due to the effect of RMsD. The former effect can be justified by comparing the corresponding spectra depicted in Figs. 7*a* and *b*, respectively, where the fundamental component shows a little decrease in amplitude (~1.5 dB) from healthy to RMsD conditions. Thus, the quasi-unsensitivity of the back-EMF space vector computed in the α_1–β_1-plane against RMsD is confirmed, which corroborate with the FEA results obtained in the previous section. Let us focus on the effect of the RMsD on the back-EMF space vector in the α_5–β_5-plane. Comparing the loci obtained under healthy (Fig. 6*b*), and RMsD (Fig. 6*d*) conditions, a very different shape can be evidenced from healthy to faulty conditions, leading to a clear qualitative fault signature. After an accurate inspection of the back-EMF space vectors spectra in the α_5–β_5-plane, from healthy (Fig. 8*a*) to RMsD (Fig. 8*b*) conditions, specific fault harmonics components have been identified as the main cause of the fault signature observed in Fig. 6*d*. Figs. 8*a* shows that according to the mathematical model, the most relevant harmonics are the fifth and the seventh inverse components, which justify the shape observed under healthy conditions in Fig. 6*b*. Now, when comparing the obtained spectrum under faulty case (Fig. 8*b*), to the reference spectrum in healthy conditions (Fig. 8*a*), it can be noted that the inverse seventh harmonic shows a relatively small variation in amplitude (~4.5 dB) from healthy to faulty conditions, whereas the fifth harmonic component shows a relevant variation in amplitude (~ 25 dB) from the healthy to faulty case. The relevant variation of the amplitude of the fifth harmonic is a specific behaviour of the machine under test. In general, the adopted fault index can detect an RMsD exploiting the variations of the fifth and seventh harmonic components of the back EMFs.

4 Validation of control signal-based detection technique of RMsD

As previously investigated and validated, based on specific harmonics tracking in the stator EMF, a potential diagnostic index for RMsD can be established. In the present section, a newly developed control signal-based detection technique of RMsD for a vector-controlled six-phase surface-mounted AC PMSM is numerically tested, then experimentally validated.

4.1 Control signal-based fault frequency tracking

Fig. 9 illustrates the adopted FOC control scheme, allowing the speed control of the six-phase PMSM. For current tracking, eight proportional–integral (PI) regulators are adopted.

Four current regulators [PI(b), PI(c), PI(d), PI(e)] are implemented on the d_1–q_1 reference frame rotating at angular speed ω, whereas four other current regulators [PI(f), PI(g), PI(h), PI(i)] are implemented on the d_5–q_5 reference frame rotating at angular speed 5ω.

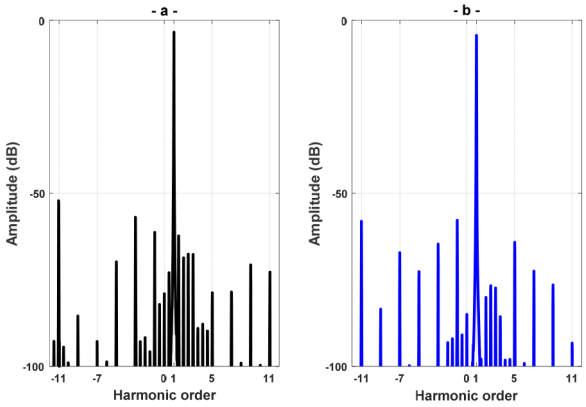

Fig. 7 *Experimental results: harmonic spectra of the back-EMF space vectors in the α_1–β_1*

(a) Healthy motor, ***(b)*** Motor with 10° of RMsD

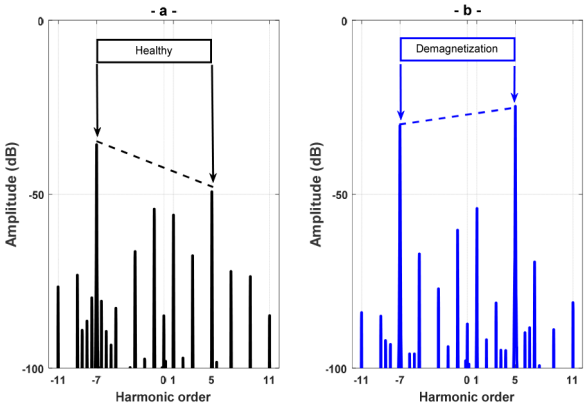

Fig. 8 *Experimental results: harmonic spectra of the back-EMF space vectors in the α_5–β_5*

(a) Healthy motor, ***(b)*** Motor with 10° of RMsD

The reference currents $i_{S5d,\mathrm{ref}}$ and $i_{S5q,}$ref are usually set to zero, whereas $i_{S1d,\mathrm{ref}}$ can be selected to optimise the system behaviour. The reference current $i_{S1q,\mathrm{ref}}$ is determined by the PI(a) of the external speed loop. At the output of the eight current regulators, the back-EMF compensation is applied, and two proper coordinate rotations calculate the reference voltage space vectors $\bar{v}_{S1,\mathrm{ref}}$, and $\bar{v}_{S5,\mathrm{ref}}$. Finally, the pulse-width modulation (PWM) block determines the gate signals of the six inverter legs using a double three-phase space-vector PWM technique.

The impact of uniform RMsD can be directly observed by analysing the time-domain waveforms of the stator voltages. More specifically, the considered uniform RMsD affects the harmonic content of the back EMFs. Therefore, for having sinusoidal stator currents, stator voltages with a certain harmonic content must be applied to stator phase windings. The reference values of these voltages are automatically generated by the current regulators implemented in the control scheme of Fig. 9. It is worth noting that the harmonic content variation is monitored not using the stator voltages generated by the inverter, but processing the reference voltages generated by the current regulators [28].

The harmonic content variation is strongly dependent on the machine design; therefore, any detection strategy of uniform RMsD should be tuned based on the machine parameters and cannot be considered valid for any machine design. However, the method proposed has a general validity because by analysing a certain set of possible machine designs it has been verified that at least one, but generally more than one harmonic is changing in case of demagnetisation phenomena. Therefore, it is possible to use the variation of a single harmonic component or a combination of them for defining an effective fault index.

4.2 Simulation results

To emphasise the performance of the proposed control signal-based approach for RMsD detection, a simulation scheme has been implemented in MATLAB/Simulink™ environment by combining the model of the six-phase PMSM previously presented, with the control system illustrated in Fig. 9, where the bandwidths of inner current loops are adjusted to 80 Hz in space 1 and 50 Hz for space 5. The implemented system allows a detailed investigation of the behaviour of the controlled six-phase PMSM under healthy and faulty conditions. A uniform demagnetisation on the trailing edges of the magnets has been simulated by reducing the pole-arc value.

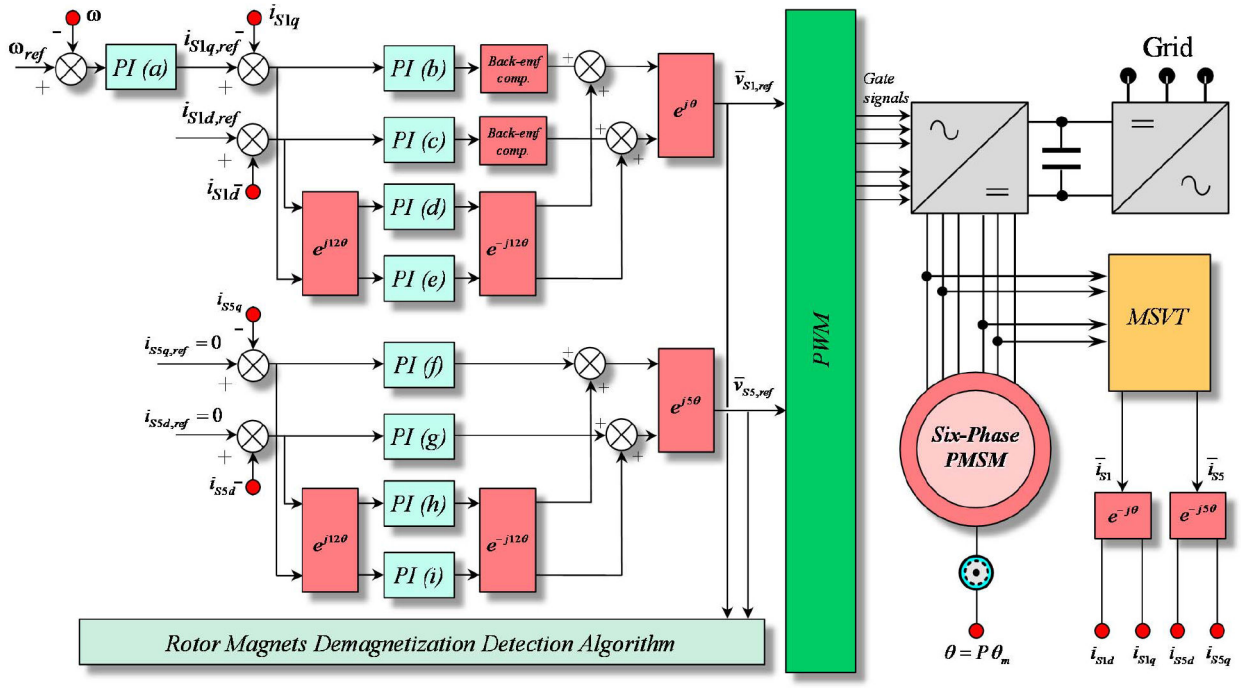

Fig. 9 *Block diagram of the vector-controlled asymmetric six-phase surface-mounted AC PM machine*

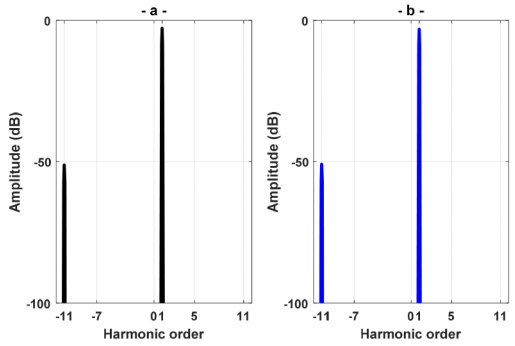

Fig. 10 *Simulation results: harmonic spectrum of the stator voltages space vector in the α_1–β_1-plane, under*
(a) Healthy, ***(b)*** Under 10° of uniform RMsD

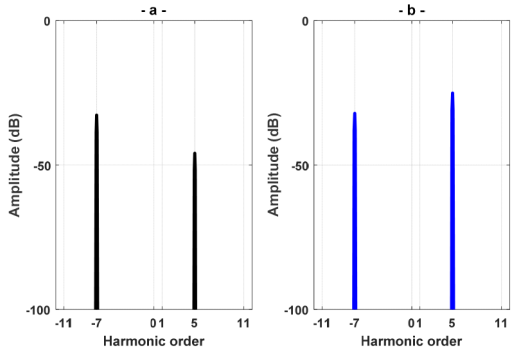

Fig. 11 *Simulation results: harmonic spectrum of the stator voltages space vector in the α_5–β_5-plane, under*
(a) Healthy, ***(b)*** Under 10° of uniform RMsD

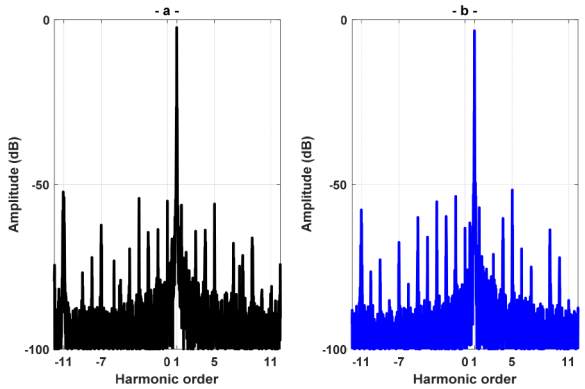

Fig. 12 *Experimental results: harmonic spectrum of the stator voltages space vector in the α_1–β_1-plane, under*
(a) Healthy, ***(b)*** Under 10° of uniform RMsD

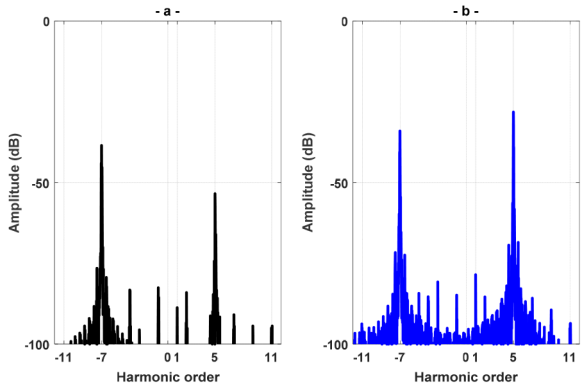

Fig. 13 *Experimental results: Simulation results: harmonic spectrum of the stator voltages space vector in the α_5–β_5-plane, under*
(a) Healthy, ***(b)*** Under 10° of uniform RMsD

The machine parameters reported in Table 1 has been adopted for the healthy case.

The simulations have been achieved, at a constant speed of 1000 rpm with a load torque of 8 Nm, around 40% of the rated torque, first under healthy magnets, then, with magnets having a reduced pole arc of 10° to reproduce RMsD.

The spectra of the stator voltage space vector in the α_1–β_1, under healthy and 10° of RMsD, are reported in Figs. 10*a* and *b*, respectively, where the content is practically unchanged. However, observing the corresponding spectra in the α_5–β_5, under healthy and 10° of RMsD, reported in Figs. 11*a* and *b*, respectively, the contribution of the fifth harmonic is evidenced with an increasing amplitude variation (~20 dB). It should also be noted that the inverse seventh harmonic shows a little amplitude variation (~2 dB) from healthy to faulty conditions.

At this point, the potential of the fifth harmonic component, derived from the space vector $\bar{v}_{S5,\,ref}$, is clearly evidenced as a sensitive fault index for RMsD detection. The aim of the next section is to confirm experimentally this result.

4.3 Experimental results

To test the feasibility and performance of the proposed RMsD detection technique, based on the reference voltage space vectors evaluated in the α_1–β_1 and α_5–β_5 planes, a complete experimental setup has been built. The six-phase AC PMSM is driven by the same DC motor, used for the tests in the previous section, which is controlled by a dual two-bridge converter.

A dSPACE system based on the DS1104 control board has been used to implement the FOC scheme illustrated by Fig. 9. The same bandwidths of the inner current loops in space 1 and space 5, adopted in simulations, have been considered for experiments. The inverter switching frequency was fixed to 4 kHz with a dead time of 2 µs, whereas a sampling rate of 10 kHz for data acquisition and spectral treatments has been adopted. All the experimental tests have been performed by operating the motor at constant speed of 1000 rpm, and the load has been adjusted so that the produced torque is 8 Nm, around 40% of the rated torque.

Figs. 12*a* and *b* show the harmonic spectra of $\bar{v}_{S1,\,ref}$ under healthy and RMsD conditions, respectively. It can be noted that the spectrum of $\bar{v}_{S1,\,ref}$, for both conditions (Fig. 12), is mainly composed of the fundamental component.

Figs. 13*a* and *b* show the harmonic spectra of $\bar{v}_{S5,\,ref}$ under healthy and RMsD conditions, respectively. It can be seen that the space vector $\bar{v}_{S5,\,ref}$ is mainly composed of the fifth and the inverse seventh harmonic components.

When comparing the two spectra (Figs. 13*a* and *b*), it can be noted that the inverse seventh harmonic shows a relatively small variation in amplitude (~3.5 dB) from healthy to faulty conditions. However, the fifth harmonic component shows a relevant variation in amplitude (~ 25 dB) from the healthy to faulty case, leading to a highly sensitive RMsD fault index in six-phase PMSM.

5 Fault quantification

Once the state of the machine is preliminarily identified by fault detection, the definition of a proper fault index providing a quantitative evaluation of the fault extending is necessary. The definition of fault indexes is generally very useful for generating alert signals in unsupervised monitoring systems.

Considering the proposed process of RMsD detection, based on motor signal analysis as well as control signal analysis, the sensitivity of the inverse seventh and fifth harmonic components of the back EMFs is validated for this type of fault. Thus, a fault index directly related to the amplitudes of these two fault harmonics was defined as

$$F_{\mathrm{i}} = \left|\frac{H_{5\mathrm{f}}}{H_{1\mathrm{f}}} - \frac{H_{5\mathrm{h}}}{H_{1\mathrm{h}}}\right| + \left|\frac{H_{7\mathrm{f}}}{H_{1\mathrm{f}}} - \frac{H_{7\mathrm{h}}}{H_{1\mathrm{h}}}\right| \tag{14}$$

where $H_{1\mathrm{f}}$ and $H_{1\mathrm{h}}$ are the amplitudes of the fundamentals evaluated in the α_1–β_1-plane under healthy and faulty conditions,

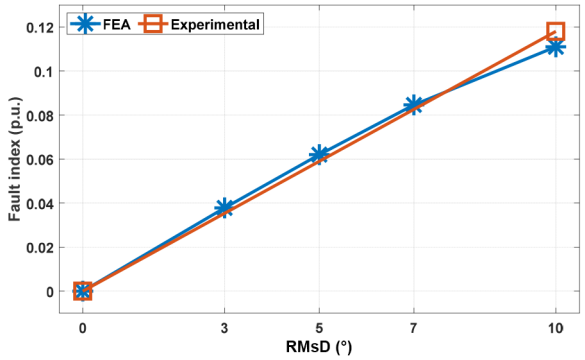

Fig. 14 *Behaviour of the fault index 'F_i' versus degree of RMsD derived from motor signal-based analysis*

respectively, H_{5h} and H_{7h} are the amplitudes of the fifth and inverse seventh harmonic components of the back EMFs, respectively, evaluated in the α_5–β_5-plane under healthy condition, and H_{5f} and H_{7f} are the corresponding amplitudes values under faulty condition. It is worth noting that the implementation of this type of fault indexes is based on linear scaling of the amplitudes; however, a decibel scaling could also be used for better emphasising the variations due to RMsD.

The fault index defined in (14), owing to the normalisation of the fault components by the fundamentals, leads to an effective insensitivity of the fault index against the operating speed. Furthermore, the fault index is not affected by temperature variations of the magnets. Temperature variations maintain unchanged the ratios between all the harmonic components.

On the basis of motor signal-based approach, the behaviour of the fault index 'F_i' versus different degrees of RMsD derived from FEA results, and the corresponding experimental results under healthy and 10° of RMsD, are represented in Fig. 14. It is shown that the magnitude of the fault index increases with the increasing severity of the RMsD. The good agreement with the experimental test under 10° of RMsD (Fig. 14) proves the good sensitivity of the proposed fault index.

6 Conclusion

In this paper, a new characterisation of uniform RMsD for six-phase surface-mounted PM synchronous motors has been presented.

The developed diagnosis technique, which is suitable for online monitoring of the rotor surface-mounted PM status, takes advantage of the intrinsic degrees of freedom of a multiphase motor drive and is based on the spectral analysis of the stator voltage space vectors calculated in the α_5–β_5-plane.

The validity of the proposed diagnosis approach was validated by experimental tests. The obtained results showed that the amplitude of the fifth harmonic component is a highly sensitive diagnostic index for uniform RMsD detection.

The results obtained are valid for the machine prototypes considered in this paper, but the approach has a general validity, i.e. analysing the harmonic behaviour in the different α–β planes, characteristics for multiphase machines, it is possible to define suitable diagnostic indexes for any machine design.

Finally, it is worth noting that the proposed diagnosis strategy could be extended to the detection of other potential failure modes for multiphase PMSMs.

7 References

[1] Levi, E.: 'Multiphase electric machines for variable-speed applications', *IEEE Trans. Ind. Electron.*, 2008, **55**, (5), pp. 1893–1909

[2] Zhao, W., Xu, L., Liu, G.: 'Overview of permanent-magnet fault-tolerant machines: topology and design', *CES Trans. Electr. Mach. Syst.*, 2018, **2**, (1), pp. 51–64

[3] Neghadari, A., Yepes, A.G., Doval-Gandoy, J., *et al.*: 'Efficiency enhancement of multiphase electric drives at light-load operation considering both converter and stator copper losses', *IEEE Trans. Power Electron.*, 2019, **34**, (2), pp. 1518–1525

[4] Duran, M.-J., Barrero, F.: 'Recent advances in the design, modeling, and control of multiphase machines – part II', *IEEE Trans. Ind. Electron.*, 2016, **63**, (1), pp. 459–468

[5] Levi, E.: 'Advances in converter control and innovative exploitation of additional degrees of freedom for multiphase machines', *IEEE Trans. Ind. Electron.*, 2016, **63**, (1), pp. 433–448

[6] Ivan, Z., Jones, M., Levi, E.: 'Arbitrary power-sharing among three-phase winding sets of multiphase machines', *IEEE Trans. Ind. Electron.*, 2018, **65**, (2), pp. 1128–1139

[7] Cao, W., Mecrow, B.C., Atkinson, G.J., *et al.*: 'Overview of electric motor technologies used for more electric aircraft (MEA)', *IEEE Trans. Ind. Electron.*, 2012, **59**, (9), pp. 3523–3531

[8] Ruoho, S., Kolehmainen, J., Ikaheimo, J., *et al.*: 'Interdependence of demagnetization, loading, and temperature rise in a permanent-magnet synchronous motor', *IEEE Trans. Magn.*, 2010, **46**, (3), pp. 949–953

[9] Zarate, S., Almandoz, G., Ugalde, G., *et al.*: 'Effects of demagnetization on torque ripples in permanent magnet synchronous machines with manufacturing tolerances'. Proc. XIII Int. Conf. Electrical Machines, Alexandroupoli, Greece, September 2018, pp. 1827–1833

[10] Faiz, J., Mazaheri-Tehrani, E.: 'Demagnetization modeling and fault diagnosing techniques in permanent magnet machines under stationary and nonstationary conditions: an Overview', *IEEE Trans. Ind. Appl.*, 2017, **53**, (3), pp. 2772–2785

[11] Choi, S., Haque, M.S., Bin Tarek, M.D.T., *et al.*: 'Fault diagnosis techniques for permanent magnet AC machine and drives – a review of current state of the art', *IEEE Trans. Transp. Electrification*, 2018, **4**, (2), pp. 444–463

[12] Fernandez, D., Hyun, D., Park, Y., *et al.*: 'Permanent magnet temperature estimation in PM synchronous motors using low-cost Hall effect sensors', *IEEE Trans. Ind. Appl.*, 2017, **53**, (5), pp. 4515–4525

[13] Reigosa, D., Fernandez, D., Yoshida, H., *et al.*: 'Permanent magnet temperature estimation in PMSMs using pulsating high-frequency current injection', *IEEE Trans. Ind. Appl.*, 2015, **51**, (4), pp. 3159–3168

[14] Kral, C., Haumer, A., Lee, S.B.: 'A practical thermal model for the estimation of permanent magnet and stator winding temperatures', *IEEE Trans. Power Electron.*, 2014, **29**, (1), pp. 455–464

[15] Hong, J., Park, S., Hyun, D., *et al.*: 'Detection and classification of rotor demagnetization and eccentricity faults for PM synchronous motors', *IEEE Trans. Ind. Appl.*, 2012, **48**, (3), pp. 923–932

[16] Ebrahimi, B.M., Faiz, J.: 'Demagnetization fault diagnosis in surface-mounted permanent magnet synchronous motors', *IEEE Trans. Magn.*, 2013, **49**, (3), pp. 1185–1192

[17] Torregrossa, D., Khoobroo, A., Fahimi, B.: 'Prediction of acoustic noise and torque pulsation in PM synchronous machines with static eccentricity and partial demagnetization using field reconstruction method', *IEEE Trans. Ind. Electron.*, 2012, **59**, (2), pp. 934–944

[18] Yang, Z., Shi, X., Krishnamurthy, M.: 'Vibration monitoring of PM synchronous machine with partial demagnetization and inter-turn short circuit faults'. Proc. IEEE Transportation Electrification Conf. Exposition, Dearborn, MI, USA, 2014, pp. 1–6

[19] Urresty, J.C., Atashkhooei, R., Riba, J.R., *et al.*: 'Shaft trajectory analysis in a partially demagnetized permanent-magnet synchronous motor', *IEEE Trans. Ind. Electron.*, 2013, **60**, (8), pp. 3454–3461

[20] Urresty, J.C., Riba, J.R., Delgado, M., *et al.*: 'Detection of demagnetization faults in surface-mounted permanent magnet synchronous motors by means of the zero-sequence voltage component', *IEEE Trans. Energy Convers.*, 2012, **27**, (1), pp. 42–51

[21] Urresty, J.C., Riba, J.R., Romeral, L.: 'A back-EMF-based method to detect magnet failures in PMSMs', *IEEE Trans. Magn.*, 2013, **49**, (1), pp. 591–598

[22] Wang, W., Zhang, J., Cheng, M., *et al.*: 'Fault-tolerant control of dual three-phase permanent-magnet synchronous machine drives under open-phase faults', *IEEE Trans. Power Electron.*, 2017, **32**, (3), pp. 2052–2063

[23] Casadei, D., Filippetti, F., Mengoni, M., *et al.*: 'Detection of magnet demagnetization in five-phase surface-mounted permanent magnet generators'. 2012 Third IEEE Int. Symp. Power Electronics for Distributed Generation Systems (PEDG), Aalborg, Denmark, 25–28 June 2012, pp. 841–848

[24] Qiu-Liang, H., Chen, Y., Li, X.: 'Fault-tolerant control strategy for five-phase PMSM with third-harmonic current injection', *IEEE Access*, 2018, **6**, pp. 58501–58509

[25] Gritli, Y., Tani, A., Rossi, C., *et al.*: 'Assessment of current and voltage signature analysis for the diagnosis of rotor magnet demagnetization in five-phase AC permanent magnet generator drives', *Math. Comput. Simul.*, 2019, **158**, pp. 91–106

[26] Bojoi, R., Cavagnino, A., Tenconi, A., *et al.*: 'Multiphase PM machine for more electric aircraft applications: prototype for design validation'. Proc. 38th Annual Conf. IEEE Industrial Electronics Society, Montreal, QC, Canada, October 2012, pp. 3628–3634

[27] Gritli, Y., Casadei, D., Tani, A., *et al.*: 'Validation of rotor magnets demagnetization detection in six-phase surface-mounted AC permanent magnet synchronous motors'. Proc. Int. Symp. Power Electronics, Electrical Drives, Automation and Motion, SPEEDAM, Amalfi, Italy, June 2018, pp. 224–229

[28] Gritli, Y., Tani, A., Rossi, C., *et al.*: 'Detection of rotor magnet demagnetization in asymmetrical six-phase surface-mounted permanent magnet synchronous motor drive'. Proc. XIII Int. Conf. Electrical Machines ICEM, Alexandroupoli, Greece, September 2018, pp. 1809–1814

8 Appendix

8.1 Appendix 1

For a given system of six real time-dependent variables x_{a1}, x_{a2}, x_{b1}, x_{b2}, x_{c1}, and x_{c2}, a new set of three space vectors $\bar{y}_1$, $\bar{y}_3$, and $\bar{y}_5$ can be defined according to the following symmetrical linear direct (15) and inverse (16) transformations:

$$\begin{cases} \bar{y}_{S1} = \frac{1}{3}\left[x_{a1} + x_{a2}\,\bar{\alpha} + x_{b1}\,\bar{\alpha}^4 + x_{b2}\,\bar{\alpha}^5 + x_{c1}\,\bar{\alpha}^8 + x_{c2}\,\bar{\alpha}^9\right] \\ \bar{y}_{S3} = \frac{1}{3}\left[x_{a1} + x_{a2}\,\bar{\alpha}^3 + x_{b1} + x_{b2}\,\bar{\alpha}^3 + x_{c1} + x_{c2}\,\bar{\alpha}^3\right] \\ \bar{y}_{S5} = \frac{1}{3}\left[x_{a1} + x_{a2}\,\bar{\alpha}^5 + x_{b1}\,\bar{\alpha}^8 + x_{b2}\,\bar{\alpha} + x_{c1}\,\bar{\alpha}^4 + x_{c2}\,\bar{\alpha}^9\right] \end{cases} \tag{15}$$

$$\begin{cases} x_{a1} = \Re_e[\bar{y}_{S3}] + \bar{y}_{S1}\cdot 1 + \bar{y}^*_{S5}\cdot 1 \\ x_{b1} = \Re_e\,[\bar{y}_{S3}] + \bar{y}_{S1}\cdot\bar{\alpha}^4 + \bar{y}^*_{S5}\cdot\bar{\alpha}^4 \\ x_{c1} = \Re_e\,[\bar{y}_{S3}] + \bar{y}_{S1}\cdot\bar{\alpha}^8 + \bar{y}^*_{S5}\cdot\bar{\alpha}^8 \\ x_{a2} = \Im_m\,[\bar{y}_{S3}] + \bar{y}_{S1}\cdot\bar{\alpha} + \bar{y}^*_{S5}\cdot\bar{\alpha}^7 \\ x_{b2} = \Im_m\,[\bar{y}_{S3}] + \bar{y}_{S1}\cdot\bar{\alpha}^5 + \bar{y}^*_{S5}\cdot\bar{\alpha}^{11} \\ x_{c2} = \Im_m\,[\bar{y}_{S3}] + \bar{y}_{S1}\cdot\bar{\alpha}^9 + \bar{y}^*_{S5}\cdot\bar{\alpha}^3 \end{cases} \tag{16}$$

where $\bar{\alpha} = e^{j\,\pi/6}$.

According to transformations (15) and (16), the obtained three space vectors can arbitrarily move in the respective planes, namely α_1–β_1, α_3–β_3, and α_5–β_5.

8.2 Appendix 2

According to the assumptions usually adopted for the electrical machine modelling, the magnetic field in the air gap, produced by the kth stator winding, can be represented as

$$h_{Sk}(\theta_S,\,t) = \sum_{\rho\,(\text{odd})\,=\,1}^{\infty} \frac{N_S\,K_{WS\rho}\,i_k}{\rho\,\pi\,\delta\,P}\,(-1)^{\frac{\rho-1}{2}}\,\Re_e\left[e^{-j\,\rho\,\theta_S} e^{j\,\rho\,\psi_K}\right] \tag{17}$$

where i_k is the kth winding current, δ is the air-gap thickness, P is the number of pole pairs, ρ is the order of the spatial harmonic, and θ_S is a stator angular coordinate in electrical radians. The arrangement of the stator winding is defined by the number of winding series-connected conductors N_S, the winding coefficients $K_{WS\rho}$ and the angular position of the magnetic axis ψ_k.

Taking into account the spatial disposition of the magnetic axes of the six stator windings (Fig. 1, $\Psi_{a1} = 0$, $\Psi_{b1} = 2\pi/3$, $\Psi_{c1} = 4\pi/3$, $\Psi_{a2} = \pi/6$, $\Psi_{b2} = 5\pi/6$, and $\Psi_{c2} = 3\pi/2$), the magnetic field in the air gap due to the stator currents can be expressed as

$$h_S(\theta_S,\,t) = \sum_{\rho(\text{odd})\,=\,1}^{\infty} \frac{3\,N_S\,K_{WS\rho}}{\rho\,\pi\,\delta\,P}\,(-1)^{\frac{\rho-1}{2}}\,\Re_e\left[\bar{i}_{S\rho} e^{-j\,\rho\,\theta_S}\right] \tag{18}$$

where

$$\bar{i}_{S\rho} = \frac{1}{3}\left(i_{a1} + i_{a2}\,\bar{\alpha}^{\rho} + i_{b1}\,\bar{\alpha}^{4\,\rho} + i_{b2}\,\bar{\alpha}^{5\,\rho} + i_{c1}\,\bar{\alpha}^{8\,\rho} + i_{c2}\,\bar{\alpha}^{9\,\rho}\right) \tag{19}$$

Limiting the magnetic-field representation up to the 11th spatial harmonic, and according to the direct transformation (15), (18) becomes

$$\begin{aligned} h_S(\theta_S,\,t) = \frac{3\,N_S}{\pi\,\delta\,P}\Re_e\Big[&K_{WS1}\bar{i}_{S1}\,e^{-j\,\theta_S} - \frac{K_{WS3}}{3}\bar{i}_{S3}\,e^{-j\,3\,\theta_S} \\ &+ \frac{K_{WS5}}{5}\bar{i}_{S5}\,e^{-j\,5\,\theta_S} - \frac{K_{WS7}}{7}\bar{i}^*_{S5}\,e^{-j\,5\,\theta_S} \\ &+ \frac{K_{WS9}}{9}\bar{i}^*_{S3}\,e^{-j\,9\,\theta_S} - \frac{K_{WS11}}{11}\bar{i}^*_{S1}\,e^{-j\,11\,\theta_S}\Big] \end{aligned} \tag{20}$$

As can be seen in (20), the direct transformation (15) leads to three current space vectors, where the subscripts 1, 3, and 5 are representing the order of the first harmonics in the corresponding magnetic-field distribution. The secondary harmonics in the magnetic-field distribution are of order 11, 9, and 7, respectively.

The magnetic field in the air gap produced by the rotor magnets, expressed in the rotor reference frame, up to the 11th spatial harmonic, is

$$h_R(\theta_R,\,t) = \sum_{\rho\,(\text{odd})\,=\,1}^{11} \Re_e\left[\bar{H}_{R\rho}\,e^{-j\,\rho\,\theta_R}\right] \tag{21}$$

where θ_R is a stator angular coordinate in electrical radians and $\bar{H}_{R\rho}$ are the constant coefficients of the Fourier expansion, which depend on the rotor magnet properties and their demagnetisation level.

The total magnetic field in the air gap, due to stator currents and rotor magnets, in the stator reference frame, can be expressed as

$$h_T(\theta_S,\,t) = \sum_{\rho(\text{odd})\,=\,1}^{\infty} \Re_e\left[\bar{h}_{T\rho}\,e^{-j\,\rho\,\theta_S}\right] \tag{22}$$

where

$$\bar{h}_{T1} = \frac{3\,N_S\,K_{WS1}}{\pi\,\delta\,P}\,\bar{i}_{S1} + \bar{H}_{R1}\,e^{j\theta} \tag{23}$$

$$\bar{h}_{T3} = -\frac{N_S\,K_{WS3}}{\pi\,\delta\,P}\,\bar{i}_{S3} + \bar{H}_{R3}\,e^{j\,3\theta} \tag{24}$$

$$\bar{h}_{T5} = \frac{3\,N_S\,K_{WS5}}{5\,\pi\,\delta\,P}\,\bar{i}_{S5} + \bar{H}_{R5}\,e^{j\,5\theta} \tag{25}$$

$$\bar{h}_{T7} = -\frac{3\,N_S\,K_{WS7}}{7\,\pi\,\delta\,P}\,\bar{i}^*_{S5} + \bar{H}_{R7}\,e^{j\,7\theta} \tag{26}$$

$$\bar{h}_{T9} = \frac{N_S\,K_{WS9}}{3\,\pi\,\delta\,P}\,\bar{i}^*_{S3} + \bar{H}_{R9}\,e^{j\,9\theta} \tag{27}$$

$$\bar{h}_{T11} = -\frac{3\,N_S\,K_{WS11}}{11\,\pi\,\delta\,P}\,\bar{i}^*_{S1} + \bar{H}_{R11}\,e^{j\,11\theta} \tag{28}$$

and θ is the rotor position in electrical radians.

In general, the linked flux with the kth stator winding, due to the air-gap magnetic field, can be determined as

$$\boldsymbol{\varphi}_{Sk} = \frac{\mu_0\,N_S\,L\,\tau}{\pi} \sum_{\rho(\text{odd})\,=\,1}^{7} \frac{K_{WS\rho}}{\rho}\,(-1)^{\frac{\rho-1}{2}}\,\Re_e\left[\bar{h}_{T\rho}\,e^{-j\,\rho\,\psi_K}\right] \tag{29}$$

where L is the stack length and τ is the pole pitch.

Substituting (23)–(28) into (29), and taking transformations (15) into account, leads to have the linkage flux space vectors $\bar{\varphi}_{S1}$, $\bar{\varphi}_{S3}$, and $\bar{\varphi}_{S5}$, where

$$\bar{\phi}_{m1} = \frac{\mu_0\,N_S\,L\,\tau\,K_{WS1}}{\pi}\,\bar{H}_{R1} \tag{30}$$

$$\bar{\phi}_{m3} = -\frac{\mu_0\,N_S\,L\,\tau}{\pi}\frac{K_{WS3}}{3}\,\bar{H}_{R3} \tag{31}$$

$$\bar{\phi}_{m5} = \frac{\mu_0 N_S L \tau}{\pi} \frac{K_{WS5}}{5} \bar{H}_{R5} \tag{32}$$

$$\bar{\phi}_{m7} = -\frac{\mu_0 N_S L \tau}{\pi} \frac{K_{WS7}}{7} \bar{H}^*_{R7} \tag{33}$$

$$\bar{\phi}_{m9} = \frac{\mu_0 N_S L \tau}{\pi} \frac{K_{WS9}}{9} \bar{H}^*_{R9} \tag{34}$$

$$\bar{\phi}_{m11} = -\frac{\mu_0 N_S L \tau}{\pi} \frac{K_{WS11}}{11} \bar{H}^*_{R11} \tag{35}$$

$$L_{S1} = L_{Sd1} + \frac{3\,\mu_0 N_S^2 L \tau}{\pi^2\,\delta P}\left(K_{WS1}^2 + \frac{K_{WS11}^2}{121}\right) \tag{36}$$

$$L_{S3} = L_{Sd3} + \frac{3\,\mu_0 N_S^2 L \tau}{\pi^2\,\delta P}\left(\frac{K_{WS3}^2}{9} + \frac{K_{WS9}^2}{81}\right) \tag{37}$$

$$L_{S5} = L_{Sd5} + \frac{3\,\mu_0 N_S^2 L \tau}{\pi^2\,\delta P}\left(\frac{K_{WS5}^2}{25} + \frac{K_{WS7}^2}{49}\right) \tag{38}$$

In (36)–(38), $L_{S\rho}$ and $L_{Sd\rho}$ are, respectively, the synchronous inductance and leakage inductance in $\alpha_\rho - \beta_\rho$-plane.